Supporting Information for: Fulgides as Light Driven Molecular Rotary Motors: Computational Design of a Prototype Compound

Michael Filatov,*,† Marco Paolino,‡ Seung Kyu Min,† and Kwang S. Kim†

†*Department of Chemistry, School of Natural Sciences, Ulsan National Institute of Science and Technology (UNIST), Ulsan 44919, Korea*

‡*Dipartimento di Biotecnologie, Chimica e Farmacia (Dipartimento di Eccellenza 2018-1022), Università di Siena, Via A. Moro 2, 53100 Siena, Italy*

E-mail: mike.filatov@gmail.com

Contents

1 Synthesis of DTMF

The DTMF molecule designed in this work can be synthesized by applying a sequence of reactions reported in the literature and presented here to propose a concrete and feasible synthetic strategy. The 5,6-dihydro-4H-cyclopenta[b]thiophen-4-one nucleus is already reported in several articles. In particular, 3,5-dimethyl-5,6-dihydro-4H-cyclopenta[b]thiophen-4-one (**2a**) was reported by Ewen et al. in a 2003 patent.[1] Moreover, this nucleus can be readily obtained by monomethylation of the methylene in α-position to the carbonyl group of 5,6-dihydro-4H-cyclopenta[b]thiophen-4-one (**1**).[2] This synthetic intermediate, which represents the stator in the final molecule, can be conjugated to the commercial product 2-Methylene succinic anhydride (**3a**) by Stobbe condensation using LDA in THF.[3]

However, under the reaction conditions, the opening of the anhydride ring can be easily predicted and the succinic acid derivative **4a** could be obtained as synthetic intermediate. Alternatively, Stobbe condensation can be carried out on the protected form of the succinic derivative **5a** obtaining the protected compound **6a**. This intermediate can be deprotected by means of a saponification reaction to obtain the diacid compound **4a** which upon ring-closure with acetyl chloride can provide the anhydride target compound DTMF, see Scheme SI-1.

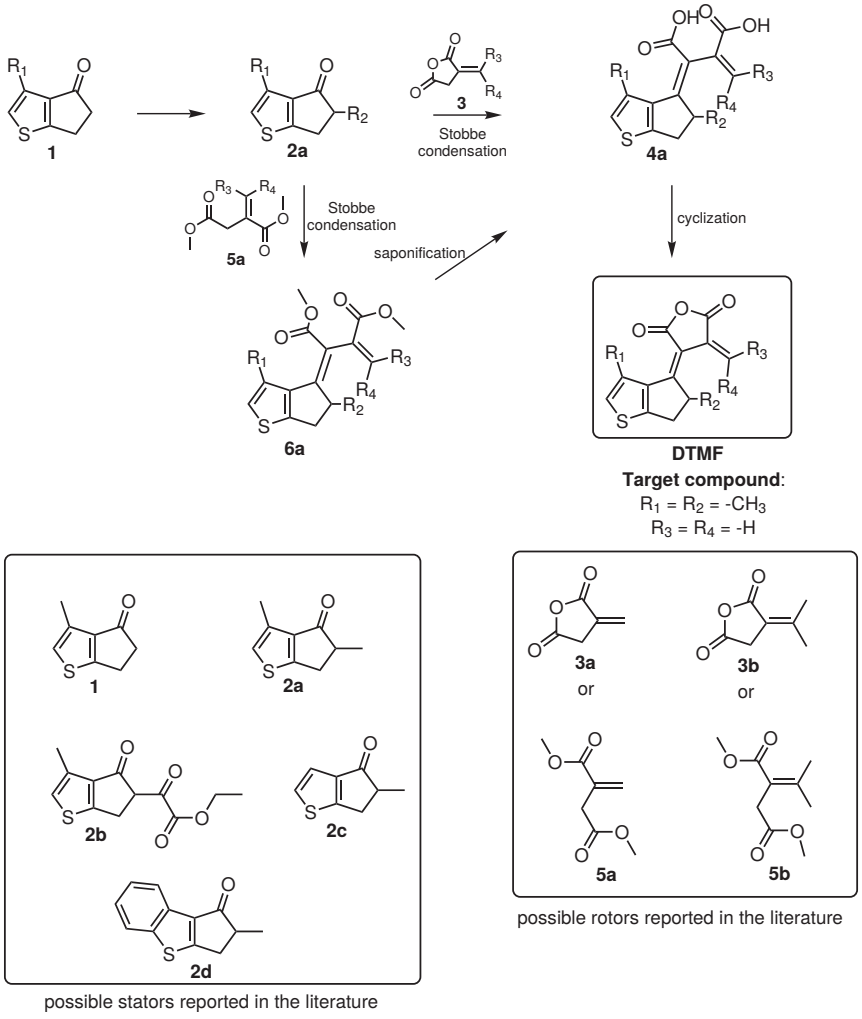

Scheme SI-1: Possible synthetic route to the DTMF motor.

This synthetic strategy can not only be pursued to obtain the DTMF target compound but also applied to combine other derivatives of 5,6-dihydro-4H-cyclopenta[b]thiophen-

4-one scaffold that could be interesting to vary the stator. For example, the achiral stator **1** without methyl group in position 5[2] or a more bulky group bearing different electronic properties such as α-keto ester in the same position (**2b**) can be used.[2] Moreover, instead of the current stator, some other interesting nuclei based on 5,6-dihydro-4H-cyclopenta[b]thiophen-4-one can be introduced by modifying the methyl in position 3 while preserving the chiral methyl in position 5. Indeed, the methyl on C3 can easily be eliminated (**2c**) as reported by Ryabov et al.,[4] or replaced with a condensed benzene in order to increase the planarity of the substituent and extend the conjugation throughout the entire structure (**2d**).[5]

Finally, the structural modification can be introduced at the anhydride rotor, thus increasing the steric hindrance on the exocyclic double bond. In this regard, many synthetic intermediates are commercially available, both in anhydride and in diester form. Certainly interesting is the introduction of two methyl groups reported in numerous fulgide compounds.[6–8]

2 Analysis of the central π-bond breaking mechanism

The homolytic/heterolytic breaking of the central π-bond of DTMF was investigated by considering fragments obtained by complete breaking of the C_4=$C_{3'}$ bond and saturating the dangling σ-bonds by methyl group, see Figure SI-1. The geometries of the obtained (5R)-3,4,5-Trimethyl-1-thia-5,6-dihydro-4H-pentalene (DT) and 3-Methyl-4-methylene-3H-furan-2,5-dione (MF) fragments were optimized using the spin-restricted KS method for the closed shell (charged) fragments and the spin-restricted open-shell KS (ROKS) method for the radical fragments. For all the fragments, the +1, 0, and -1 overall charges were considered. The calculations employ the 6-31G* basis set and the BH&HLYP density functional.

The energies of the Lewis structures obtained by homolytic/heterolytic breaking of the central π-bond are reported in Table SI-1. The energies were estimated using the obtained energies of the fragments less the total energy of ethylene (BH&HLYP/6-31G*: -79.768781 a.u.) and including an electrostatic interaction between the charged fragments. The latter energy was estimated as follows. The centers of the positive/negative charge in the fragments were calculated using the Mulliken atomic charges at the optimized geometry of the fragments. The fragments were aligned with the respective blades of the *E*P-DTMF motor and the distance between the charge centers was measured. The interaction energy between the ± 1 point charges was calculated using the obtained distance.

The total energies of the Lewis structures reported in Table SI-1 indicate that the homolytic breaking of the central π-bond and the heterolytic breaking resulting in charge transfer to the MF fragment are nearly isoenergetic, the energy difference 2.5 kcal/mol. The heterolytic breaking with charge transfer to the DT unit is energetically disfavored

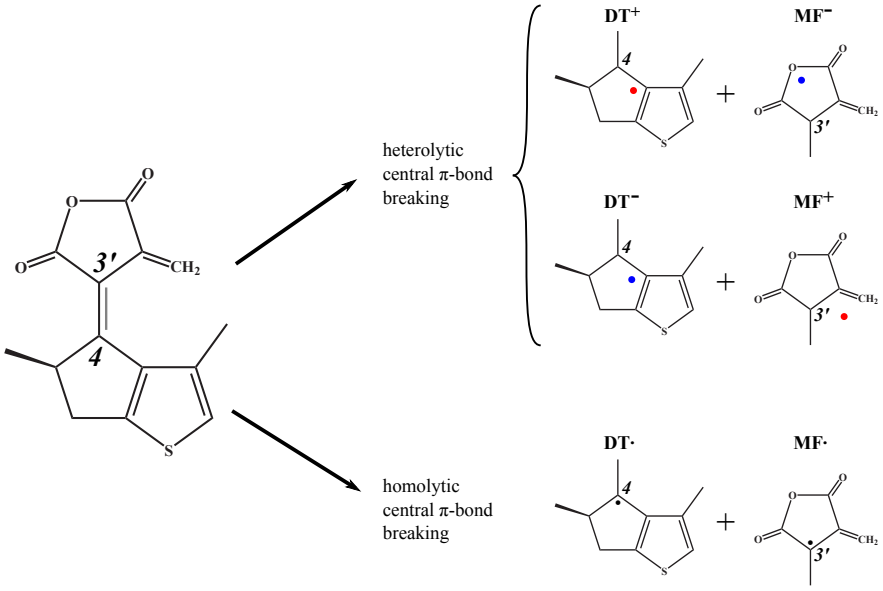

Figure SI-1: Fragments obtained by complete breaking of the central C=C bond of *E*P-DTMF and saturating the dangling σ-bonds by methyl groups. The red/blue dots in the Lewis structures show location of the center of the positive/negative charge on the fragments.

Table SI-1: Total energies (in hartree atomic units, a.u.) of the fragments shown in Figure SI-1 and the estimated total energies of the Lewis structures obtained by heterolytic and homolytic breaking of the central π-bond. The total energy of the *E*P-DTMF molecule obtained by the SSR-BH&HLYP/6-31G* method is -1164.097200 a.u.

charge	DT	MF		$R_{\pm Q}$[a]	$E_{\pm Q}$[b]	E_{tot}[c]
+1	-786.568017	-456.722048	DT^{+}–MF^{-}	4.163	-0.1271	-1164.030593
0	-786.768739	-457.034544	$DT^{\bullet}$–$MF^{\bullet}$	–	–	-1164.034502
-1	-786.751132	-457.104242	DT^{-}–MF^{+}	2.508	-0.2110	-1163.915395

[a] Distance (Å) between the centers of the positive/negative charge on the fragments shown in Figure SI-1.
[b] Electrostatic energy (a.u.) of the charges.
[c] Estimated total energy (a.u.) of the Lewis structures. The energy is obtained as a sum of the respective fragment energies, the electrostatic energy, and less the total energy of ethylene, -79.768781 a.u.

by *ca.* 75 kcal/mol. The energy of the central π-bond of the *E*P-DTMF conformation estimated from the energy of the homolytic Lewis structure and the total energy of *E*P-DTMF is 39.3 kcal/mol. The near energetic equality of the homolytic and heterolytic π-bond breaking suggests that the conical intersections between the S_1 and S_0 states can be achieved by torsion and bond_length_alternation (BLA) distortion and do not require any pyramidalization distortion.[9]

3 Cyclization reaction

Photochromism of fulgides is caused by the photochemically activated electrocyclization reaction,[10,11] see Scheme SI-2. For example, in thienylfulgide (**2**) the 1,3,5-hexatriene motif (shown in blue in Scheme SI-2) undergoes facile 6π-electrocyclization to 1,3-cycloxehadiene (red in Scheme SI-2);[10] stable closed-shell molecule.

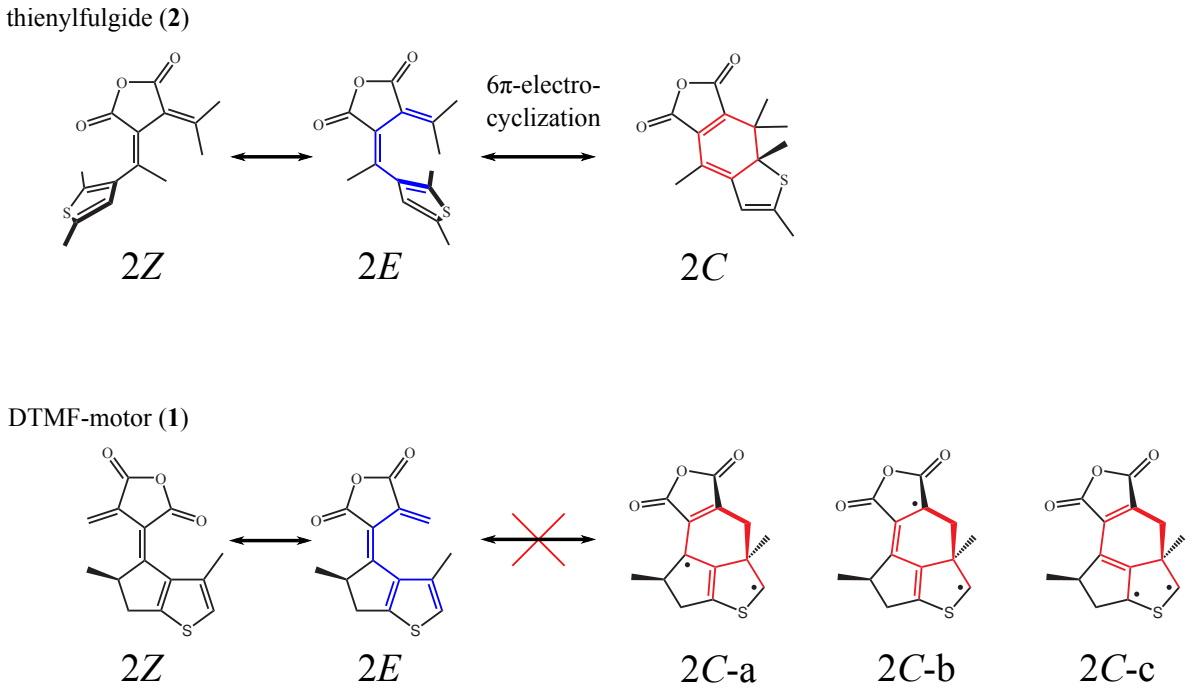

Scheme SI-2: *E*/*Z* isomerization and cyclization of the usual fulgides and the DTMF motor.

In DTMF (**1**), the hexatriene motif is replaced by a methylene-heptatriene motif (blue in Scheme SI-2). When forced to cyclize, the latter motif acquires an open-shell electronic structure represented by three biradical Lewis structures in Scheme SI-2. The cyclohexene/hexadiene motifs shown in red in structures **2***C*-a – **2***C*-c have unsaturated valences

which cannot be eliminated without considerable rearrangement of the chemical structure of the cyclic form. As cyclization of DTMF (and related compounds) leads to chemically unstable conformation, this process is blocked by the design of the DTMF's stator blade (the thiapentalene moiety).

4 Computational methods

4.1 SSR method

The SSR method[12–17] employed in this work to obtain the ground and excited electronic states energies, forces on the nuclei (the analytic gradient), and the non-adiabatic coupling (NAC) vector employs ground state eDFT[18–23] to describe the non-dynamic electron correlation occurring due to multireference character of the ground state and eDFT for ensembles of ground and excited states[24–27] to obtain excitation energies from a variational time-independent formalism. The ensemble representation of the density and energy of a strongly correlated electronic state results in occurrence of the fractional occupation numbers (FONs) of several frontier KS orbitals. Here, the SSR(2,2) method is used, where two fractionally occupied orbitals accommodate two electrons in total. The energies of the ground S_0 and excited S_1 states are obtained in SSR(2,2) from variational optimization of an ensemble of a perfectly spin-paired singlet (PPS) electronic configuration and an open-shell singlet (OSS) configuration with respect to the KS orbitals and their FONs (the SA-REKS(2,2)[14] orbital optimization), which is followed by solving a 2×2 secular problem

$$\begin{pmatrix} E_0^{PPS} & \Delta_{01}^{SA} \\ \Delta_{01}^{SA} & E_1^{OSS} \end{pmatrix} \begin{pmatrix} a_{00} & a_{01} \\ a_{10} & a_{11} \end{pmatrix} = \begin{pmatrix} E_{S_0} & 0 \\ 0 & E_{S_1} \end{pmatrix} \begin{pmatrix} a_{00} & a_{01} \\ a_{10} & a_{11} \end{pmatrix} \tag{SI-1}$$

for the actual S_0 and S_1 states.[15–17] The interstate coupling parameter Δ_{01}^{SA} is calculated simultaneously with the E_0^{PPS} and E_1^{OSS} energies when optimizing the KS orbitals (and their FONs) in the SA-REKS(2,2) calculation.[15–17]

The analytic gradients of the S_0 and S_1 energies are calculated using the formalism of Ref. 28. The gradients of the S_0 and S_1 states are related to the gradients of the PPS and OSS states and the coupling element Δ_{01}^{SA} as

$$\boldsymbol{\nabla} E_{S_k} = a_{kk}^2 \boldsymbol{\nabla} E_0^{PPS} + a_{lk}^2 \boldsymbol{\nabla} E_1^{OSS} + 2\, a_{kk}\, a_{lk}\, \boldsymbol{\nabla} \Delta_{01}^{SA}\,; \quad l \neq k\,; \quad l,k = 0,1 \tag{SI-2}$$

From the gradients $\boldsymbol{\nabla} E_{S_k}$ and $\boldsymbol{\nabla} \Delta_{01}^{SA}$, the NAC vector $\mathbf{H}_{01}$ between S_0 and S_1 is calculated as

$$\mathbf{H}_{01} = \frac{1}{E_{S_1} - E_{S_0}} \left(\frac{2\, a_{00}\, a_{01}\, \mathbf{G}_{01} + \mathbf{h}_{01}}{a_{00}\, a_{11} + a_{01}\, a_{10}} \right), \tag{SI-3}$$

where

$$\mathbf{G}_{01} = \frac{1}{2}(\boldsymbol{\nabla} E_{S_0} - \boldsymbol{\nabla} E_{S_1}) \tag{SI-4}$$

$$\mathbf{h}_{01} = \boldsymbol{\nabla} \Delta_{01}^{SA} \tag{SI-5}$$

$$\mathbf{g}_{01} = \frac{1}{2}(\boldsymbol{\nabla} E_0^{PPS} - \boldsymbol{\nabla} E_1^{OSS})\,. \tag{SI-6}$$

4.2 DISH-XF method

A detailed description of the DISH-XF method[29] can be found in the original article and the references cited therein. Here, a brief account of its basic features is given. The DISH-XF method combines the electronic equations derived from the exact factorization of the electronic-nuclear wavefunction[30–34] with the conventional TSH formalism.[35] The exact factorization enables one to seamlessly incorporate the effect of nuclear quantum momentum, which depends on the shape of nuclear distribution, into the classical equations of motion for the nuclei.

DISH-XF is a mixed quantum-classical method where the electronic degrees of freedom are treated quantum mechanically and the classical description in terms of trajectories is used for the nuclear degrees of freedom. For a given nuclear trajectory $\mathbf{R}^{(I)}$, the time-dependent electronic wavefunction $\Phi_{\mathbf{R}^{(\mathbf{I})}}(\mathbf{r}, t)$ is expanded in terms of the wavefunctions of the Born-Oppenheimer (BO) states as $\Phi_{\mathbf{R}^{(\mathbf{I})}}(\mathbf{r}, t) = \sum_l C_l^{(I)}(t)\phi_l(\mathbf{r}; \mathbf{R}^{(I)}(t))$ and the time evolution of an element $\rho_{lk}^{(I)}(t) = C_l^{(I)*}(t)C_k^{(I)}(t)$ of the reduced density matrix $\rho^{(I)}(t)$ is described by

$$\begin{aligned}\frac{d}{dt}\rho_{lk}^{(I)}(t) =& \frac{i}{\hbar}\left\{E_l^{(I)}(t) - E_k^{(I)}(t)\right\}\rho_{lk}^{(I)}(t) - \sum_j \left\{\sigma_{lj}^{(I)}(t)\rho_{jk}^{(I)}(t) - \rho_{lj}^{(I)}(t)\sigma_{jk}^{(I)}(t)\right\} \\ &+ \sum_j \left\{Q_{jl}^{(I)}(t) + Q_{jk}^{(I)}(t)\right\}\rho_{lj}^{(I)}(t)\rho_{jk}^{(I)}(t)\end{aligned} \tag{SI-7}$$

where $E_l^{(I)}$ and $\phi_l(\mathbf{r}; \mathbf{R}^{(I)}(t))$ are the energy and the wavefunction of the l-th BO state, $\sigma_{jk}^{(I)}$ is a non-adiabatic coupling matrix element between the jth and kth BO electronic states, and $Q_{jk}^{(I)}$ is a term that gives quantum correction to the nuclear motion arising from electronic-nuclear correlations;[32–34] the latter term is derived from the exact factorization of the electronic-nuclear wavefunction.[29] In Eq. (SI-7),the superscript (I) indicates a quantity obtained at the nuclear configuration $\mathbf{R}^{(I)}$.

In Eq. (SI-7), the $Q_{jk}^{(I)}$ term yields coupling between the nuclear quantum momenta

$i\hbar\nabla_\nu|\chi|/|\chi|$ and the electronic phases $\mathbf{f}_{\nu,j}^{(I)}$ and $\mathbf{f}_{\nu,k}^{(I)}$

$$Q_{jk}^{(I)} = \sum_\nu \frac{i\hbar}{M_\nu} \frac{\nabla_\nu|\chi|}{|\chi|}\bigg|_{\mathbf{R}^{(I)}(t)} \cdot \left(\mathbf{f}_{\nu,j}^{(I)} - \mathbf{f}_{\nu,k}^{(I)}\right) \tag{SI-8}$$

where M_ν is a mass of the νth nucleus. The nuclear quantum momenta are obtained from a number of auxiliary nuclear trajectories generated for electronic states other than the running state l. Although the concept of auxiliary trajectories for decoherence-induced surface hopping dynamics is not new,[36] the correction used here is derived from the exact quantum equations and no further renormalization of the electronic density matrix is needed.

An auxiliary trajectory $\mathbf{R}^{(I)}(t')$ is generated when a nonzero $\rho_{kk}(t')$ is encountered at a time t' and is evolved classically with a uniform velocity obtained from the energy conservation law. The electronic phase term $\mathbf{f}_{\nu,k}^{(I)} = -\int^t \nabla_\nu E_k^{(I)}(t')dt'$ is evaluated by time integration of the momentum changes at the kth BO state. To calculate the quantum momentum, a fictitious Gaussian nuclear density $|\chi_k|^2$ with a uniform variance σ is associated with the auxiliary trajectory at each BO state. Then, the nuclear quantum momentum is $\nabla_\nu|\chi|/|\chi|(\mathbf{R}^{(\mathbf{I})}(\mathbf{t})) = -\frac{1}{2\sigma^2}(R_\nu^{(I)}(t) - \langle R_\nu^{(I)}(t)\rangle)$, where $\langle R_\nu^{(I)}(t)\rangle = \sum_k \rho_{kk}^{(I)} R_{k\nu}^{(I)}(t)$. The uniform variance σ can be either obtained from the initial distribution of nuclear trajectories or set as a parameter. Here, a uniform value $\sigma = 0.1$ a.u. is used.

Nuclear trajectories follow the Newtonian equations of motion on the PES of the running state l, *i.e.*, the force on the νth nucleus is $\mathbf{F}_\nu^{(I)} = -\nabla_\nu E_l^{(I)}$. When the surface hop probability becomes greater than a random number, a surface hop is initiated. The surface hop probability from the running state l to another state $k(\neq l)$ at a time interval $[t, t+\Delta t]$ is calculated as

$$P_{l\to k} = \frac{2\Re\left[\rho_{lk}^{(I)}(t)\sigma_{lk}^{(I)}(t)\right]}{\rho_{ll}^{(I)}(t)}\Delta t\,, \tag{SI-9}$$

where the same constraints as in the Tully's fewest switches algorithm[35,37] are imposed on the hopping transition; *i.e.*, when $E_k^{(I)}$ is greater than the total energy, the transition is forbidden and, when a negative hopping probability is obtained (*e.g.*, due to the phase factor of $\rho_{lk}^{(I)}(t)$), the probability is set to zero. Upon a successful surface hop, the nuclear velocities are rescaled to satisfy the total energy conservation, and the running state is switched to the new state.

4.3 Computational details

All the quantum chemical computations are carried out using the beta-testing version of the TeraChem® program[38–43] (v1.92P, release 7f19a3bb8334), which implements the SSR method and the analytic derivatives formalism.[28] All the calculations employ the 6-31G* basis set[44] and the BH&HLYP exchange-correlation density functional.[45–47] The geometry optimizations are performed using the DL-FIND module[48] interfaced with TeraChem®. The geometries of the conical intersections are optimized by the CIOpt program[49] with the penalty function formalism and using the analytic energy gradients of the intersecting states.

The minimum energy pathways (MEPs) are obtained using the nudged elastic band (NEB) method with fixed end points.[48] The NEB method has an advantage that it converges to a MEP provided that sufficient number of discrete images are used.[50] For the S_0 and S_1 states, the following MEPs are optimized: *E*P S_0min $\rightarrow$ CI_90, CI_{90} $\rightarrow$ *Z*P S_0min, *Z*P S_0min $\rightarrow$ CI_{270}, CI_{270} $\rightarrow$ *E*P S_0min; when joined, the MEPs complete a full loop of the motor. The *E*P S_0min $\rightarrow$ CI_{90} and *Z*P S_0min $\rightarrow$ CI_{270} legs of the total MEP comprise 40 discrete images, and the other two legs comprise 60 images.

The NAMD simulations are performed by the UNI-xMD program, a standalone code which implements the DISH-XF method.[29] When calculating the NAC vector, the gradients $\boldsymbol{\nabla} E_{S_k}$ ($k = 0, 1$) and $\boldsymbol{\nabla} \Delta_{SA}$ are calculated by the TeraChem® program and then picked up by an external script that implements Eq. (SI-3); the calculated NAC vectors, analytic gradients, and the S_1 and S_0 energies are parsed to the UNI-xMD code. The nuclear equations of motion are integrated using the velocity-Verlet algorithm with the time step of 20 a.u. (0.48 fs). The electronic equations of motion (SI-7) are integrated by the 4-th order Runge-Kutta method with the time step of 0.002 a.u. (4.8×10^{-5} fs). When integrating the electronic equations of motion, the electronic energies $E_l^{(I)}$ and the non-adiabatic $\sigma_{lk}^{(I)}$ couplings are linearly interpolated between the end points of the integration interval of the nuclear equations of motion.

The initial conditions at the start of the NAMD trajectories are set up by sampling the Wigner function of a canonical ensemble at T = 300K.[51,52] The trajectories starting at the *E*P conformation were propagated for 800 steps (384 fs) and the trajectories starting at the *Z*P conformation for 1000 steps (480 fs). To simulate dissipation of the total energy, when the motor molecule works under the load (*i.e.*, produces some work on the surrounding molecules during the isomerization stage), the nuclear velocities were rescaled at the intervals of 200 steps to match the nuclear kinetic energy at T=300K.

5 Vertical excitation energies and frontier orbitals of *E*P and *Z*P conformations

At the equilibrium geometries of the S_0 conformations of DTMF optimized by the SSR-BH&HLYP/6-31G* method, the vertical excitation energies were calculated by TD-DFT, TD-BH&HLYP/6-31G*. Table SI-2 reports the two lowest excitation energies obtained in TD-DFT calculations and compares with the excitation energies obtained by SSR. The S_1 excited state corresponds to a $\pi \rightarrow \pi^*$ transition centered around the C_4=$C_{3'}$ bond, as evidenced by the orbitals shown in Figure SI-2. For SSR, the two fractionally occupied natural orbitals obtained from the relaxed density matrix of the S_1 state are shown along with the respective occupation numbers. For TD-DFT, the frontier orbitals obtained in the conventional KS calculation are shown in Figure SI-2.

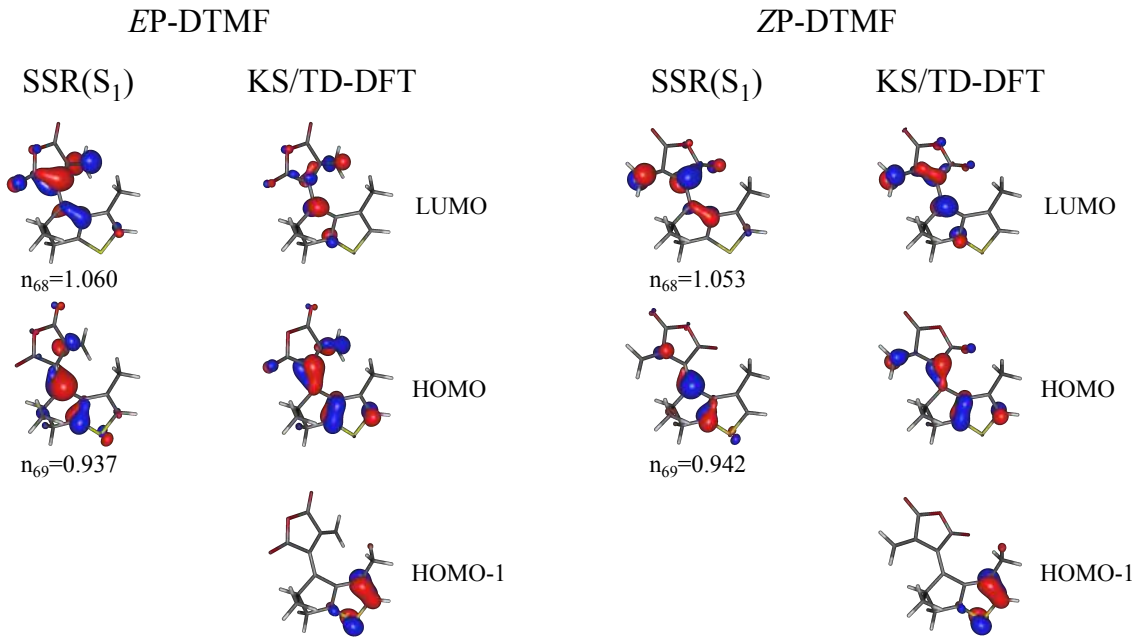

Figure SI-2: Fractionally occupied SSR natural orbitals for the S_1 state and frontier orbitals of KS/TD-DFT.

According to TD-DFT the S_1 state is a $\pi \rightarrow \pi^*$ (HOMO $\rightarrow$ LUMO) transition and the S_2 state is a HOMO-1 $\rightarrow$ LUMO transition, see Figure SI-2. The S_2 state lies *ca.* 0.6–0.9 eV above the S_1 state and has a very low oscillator strength. Hence, it's unlikely that S_2 can be involved in the photochemistry of DTMF.

The UV absorption spectra of the *E*P and *Z*P conformers were simulated theoretically by convolution of the vertical excitations calculated at one hundred geometries ob-

Table SI-2: Vertical excitation energies (eV) of the ground state equilibrium conformations of DTMF motor obtained in the SSR-BH&HLYP/6-31G* and TD-BH&HLYP/6-31G* calculations. Oscillator strengths of the transitions are given in parentheses.

	SSR	TD-DFT	
conformation	$S_1 \leftarrow S_0$	$S_1 \leftarrow S_0$	$S_2 \leftarrow S_0$
*E*P	4.02 (0.35)	4.09 (0.33)	4.92 (0.04)
*E*M	3.87 (0.33)	3.98 (0.36)	4.86 (0.03)
*Z*P	3.99 (0.44)	4.08 (0.42)	4.69 (0.09)
*Z*M	3.80 (0.40)	3.93 (0.44)	4.61 (0.06)

tained from sampling the Wigner function of the respective conformer at T=300K. The Lorentzian lineshape $L(\lambda;\lambda_i,f_{\lambda_i}) = f_{\lambda_i}\,\frac{\sigma^2}{\sigma^2+(\lambda-\lambda_i)}$, centered around the calculated excitation wavelengths λ_i with an amplitude given by the respective oscillator strength f_{λ_i} and broadened by a uniform width σ = 10 nm was used to simulate the spectra. For TD-DFT, four lowest excited states were used; for SSR, the S_1 state only was included. The resulting absorption spectra are shown in Figure SI-3. Both methods, SSR and TD-DFT, predict very close absorption maxima for the $S_1 \leftarrow S_0$ transition; 318 nm (SSR) and 314 nm (TD-DFT) for the *E*P conformation and 318 nm (SSR) and 312 nm (TD-DFT) for the *Z*P conformation. However, at wavelengths in the range 340–360 nm typically employed in the experimental measurements on molecular motors, the absorbance of DTMF drops by only a half. Hence, the DTMF motor can possibly operate at these wavelengths.

The emission spectra, see Figure 3 of the main article, were simulated by the SSR method using the approach outlined in Ref. 53. The emission intensity

$$I_{ems}(\lambda,t) \propto \frac{1}{\lambda^3}\sum_{k}^{N_{S_1}^t} L(\lambda;\lambda_k,f_{\lambda_k}) \tag{SI-10}$$

where $N_{S_1}^t$ is the number of trajectories residing in the S_1 state at an instance t and λ_k and f_{λ_k} are the absorption wavelength and the oscillator strength of the $S_1 \leftarrow S_0$ transition of k-th trajectory. The calculated emission intensities shown in Figure 3 of the main article were then renormalized so as to make the maximum intensity equal to unity.

6 Cartesian coordinates of the S_0 and S_1 species and MECI points

Cartesian coordinates and total energies of the species reported in the main article.

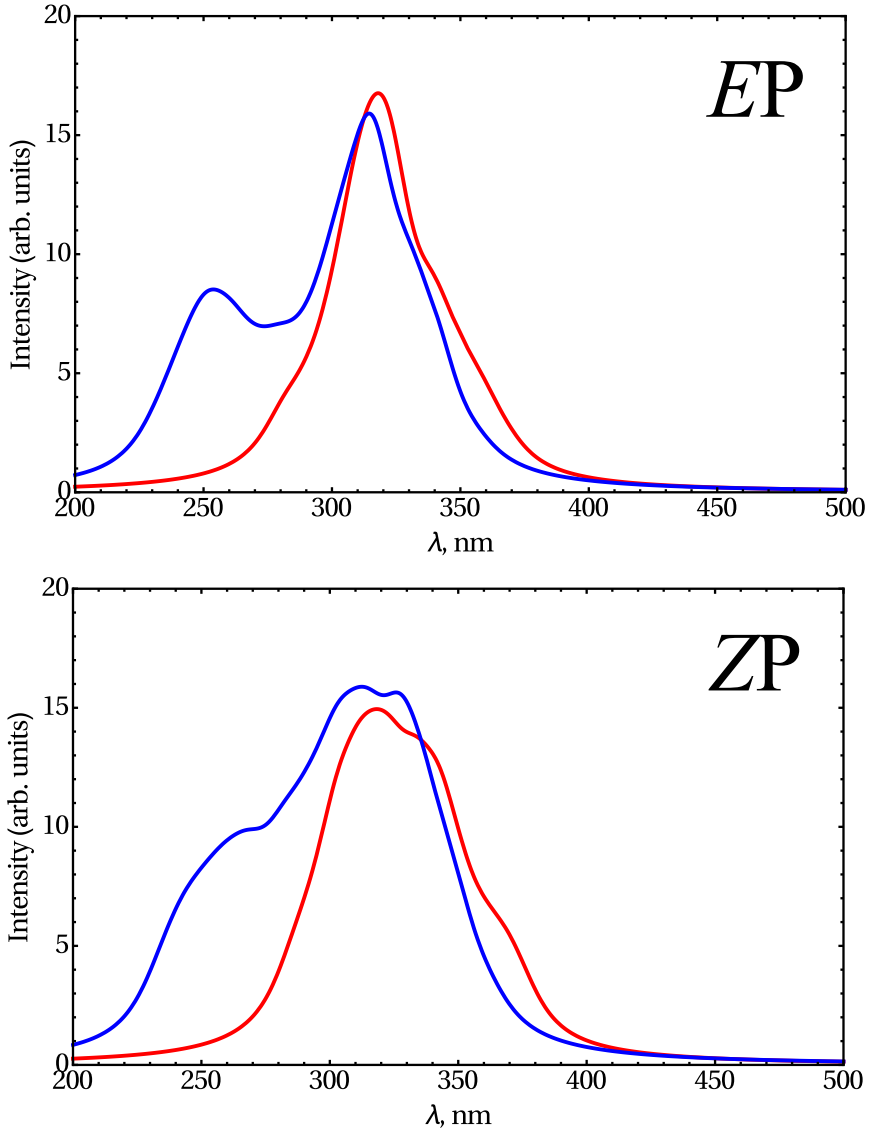

Figure SI-3: Theoretical absorption spectra of the *E*P (upper panel) and *Z*P (lower panel) conformations of DTMF simulated by the SSR-BH&HLYP/6-31G* method (red lines) and the TD-BH&HLYP/6-31G* method (blue lines).

Table SI-3: Cartesian coordinates (Å) and S_0 and S_1 total energies (hartree a.u.) of equilibrium conformations of DTMF obtained in SSR-BH&HLYP/6-31G* calculations.

	X	Y	Z	X	Y	Z	X	Y	Z	X	Y	Z
	*E*P conformation			*E*M conformation			*Z*P conformation			*Z*M conformation		
C	2.342064	3.057884	-1.701411	2.933347	3.104039	-0.722343	2.420644	3.267924	-0.714727	2.629386	2.858580	-1.364805
C	1.040453	2.289146	-2.059362	1.465343	3.304279	-0.269893	0.993665	2.788753	-1.082443	1.102323	2.788508	-1.119530
C	0.623766	1.672602	-0.727244	0.881885	1.896197	-0.105059	0.759585	1.607601	-0.151876	0.854809	1.486504	-0.354128
H	2.123423	4.098199	-1.463533	3.643945	3.573172	-0.044937	2.382201	4.062191	0.029539	3.075697	3.766526	-0.964444
H	3.060507	3.053062	-2.516661	3.099850	3.539755	-1.705872	2.963592	3.650952	-1.574979	2.850382	2.843308	-2.430464
H	0.272844	2.957144	-2.427248	1.426807	3.817727	0.686747	0.264840	3.569473	-0.888328	0.803382	3.632662	-0.499719
C	-0.658219	1.463506	-0.363237	-0.418386	1.679969	0.195580	-0.465224	1.291270	0.323206	-0.394958	1.057483	-0.058587
C	1.302690	1.219371	-3.121211	0.699397	4.139079	-1.296929	0.922186	2.368905	-2.553203	0.347806	2.836345	-2.449207
H	2.079596	0.531101	-2.796689	0.700667	3.646224	-2.267146	1.705873	1.650583	-2.779695	0.682710	2.026587	-3.092654
C	-1.278242	1.231558	0.937408	-1.295144	0.532335	-0.001000	-1.779244	1.814527	-0.049200	-1.654074	1.799068	0.016141
C	-2.706356	0.935060	0.663629	-2.511635	0.796927	0.802628	-2.745868	1.199275	0.898813	-2.693052	0.802129	0.384119
O	-2.931862	1.139069	-0.669596	-2.425049	2.074517	1.284783	-2.051306	0.419286	1.774643	-2.109227	-0.428656	0.435191
C	-1.780469	1.505271	-1.324646	-1.247109	2.676957	0.908460	-0.701458	0.451211	1.513376	-0.767350	-0.355271	0.141773
O	-3.570425	0.610459	1.409747	-3.452819	0.103964	1.010466	-3.926409	1.314694	0.949432	-3.847434	0.967581	0.608660
O	-1.800728	1.756151	-2.488117	-1.017511	3.799529	1.231667	0.063847	-0.080985	2.249709	-0.135220	-1.348713	-0.020856
C	-0.871880	1.453477	2.183699	-1.285833	-0.446422	-0.902126	-2.243187	2.617244	-1.004584	-1.999672	3.081663	-0.073139
H	0.120281	1.797522	2.415876	-0.479941	-0.572671	-1.603644	-1.627526	3.080181	-1.752045	-1.312983	3.870387	-0.319049
H	-1.565127	1.315297	2.996424	-2.120646	-1.124588	-0.958543	-3.302365	2.809475	-1.042160	-3.025499	3.352582	0.111613
C	3.664323	0.924007	1.321373	3.502782	-0.757630	-0.465476	4.026204	-0.078534	0.555561	4.064634	-0.120041	0.716363
S	4.308422	2.158870	0.289671	4.430736	0.621596	-0.949114	4.600581	1.495489	0.109323	4.698932	1.119653	-0.314262
C	2.807833	2.304439	-0.503499	3.077373	1.628068	-0.721541	3.003410	2.015872	-0.159350	3.121831	1.650421	-0.661517
C	1.850957	1.492853	0.036835	1.952806	0.939935	-0.352980	2.076184	1.056050	0.142036	2.150481	0.885263	-0.070419
C	2.359690	0.640195	1.086040	2.217611	-0.471197	-0.146462	2.677936	-0.201573	0.528630	2.713102	-0.139871	0.791183
H	4.312333	0.431844	2.022505	3.980965	-1.716749	-0.394000	4.736057	-0.850883	0.785742	4.743247	-0.757843	1.251097
H	0.398315	0.659076	-3.329370	-0.323375	4.313155	-0.991940	-0.030152	1.906849	-2.795982	-0.724072	2.743444	-2.327538
H	1.627947	1.689003	-4.046255	1.180237	5.107774	-1.412321	1.056209	3.233088	-3.199473	0.551706	3.775917	-2.957501
C	1.662340	-0.522559	1.724353	1.327610	-1.507003	0.470492	1.997925	-1.519349	0.738670	2.013397	-1.041207	1.761318
H	1.159983	-1.126591	0.972434	0.592664	-1.905256	-0.221248	1.166814	-1.642617	0.048639	1.539637	-1.881597	1.271501
H	2.382130	-1.154204	2.235296	1.928056	-2.337419	0.828785	2.699939	-2.329024	0.562352	2.727351	-1.411529	2.490730
H	0.907211	-0.227413	2.444889	0.779165	-1.100864	1.315067	1.598850	-1.612528	1.740474	1.236529	-0.504483	2.300234
$E(S_0)$		-1164.097199			-1164.091709			-1164.096570			-1164.091135	
$E(S_1)$		-1163.949437			-1163.949390			-1163.949851			-1163.951598	

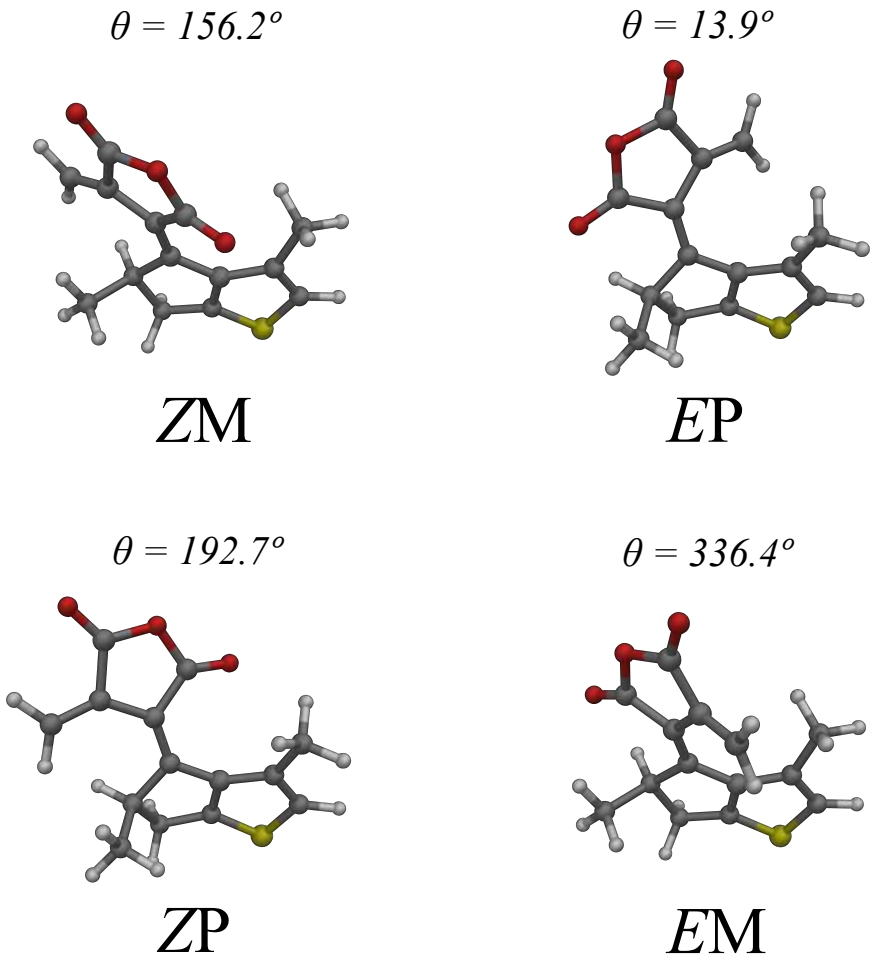

Figure SI-4: Molecular geometries of the ground state minima. For definition of the central dihedral angle θ, see Scheme 1 of the main text.

Table SI-4: Cartesian coordinates (Å), branching plane vectors (hartree/bohr) and total energies (hartree a.u.) of S_1/S_0 MECI points of DTMF obtained in SSR-BH&HLYP/6-31G* calculations.

	Cartesian coordinates			**g**-vector			**h**-vector		
	X	Y	Z	X	Y	Z	X	Y	Z
					CI_{90}				
C	2.657861	2.880386	-1.593348	0.042394	-0.012621	0.012921	0.005955	-0.021046	-0.022851
C	1.125245	2.639836	-1.646150	-0.149866	0.025851	-0.037432	0.070910	-0.276575	-0.242124
C	0.849064	1.568102	-0.608826	0.080140	0.007953	-0.053804	0.024322	-0.014621	0.046519
H	2.898163	3.916548	-1.365412	-0.015228	0.010976	-0.013161	-0.022858	-0.001171	0.001599
H	3.135938	2.649827	-2.545490	-0.011502	0.007316	-0.021962	0.020171	0.005902	0.002725
H	0.604036	3.539052	-1.314095	0.026763	0.045981	-0.046321	-0.013763	-0.044496	0.055004
C	-0.456254	1.062872	-0.310429	0.128250	0.384925	0.265910	-0.046027	0.018354	-0.048651
C	0.602240	2.287377	-3.039511	0.050935	0.039440	0.030385	-0.000019	0.043171	-0.030429
H	1.074947	1.385547	-3.418317	0.003360	-0.002273	0.000909	0.001113	0.007504	0.006302
C	-1.382137	1.576507	0.640239	-0.067709	-0.271602	-0.175183	0.206136	-0.296761	0.296007
C	-2.567974	0.670926	0.557844	-0.100251	0.028761	0.078025	-0.002130	-0.009170	-0.008871
O	-2.299275	-0.298115	-0.354750	0.070772	-0.016739	-0.050954	0.039431	-0.061445	0.087045
C	-1.033292	-0.107838	-0.909759	-0.270993	-0.459445	-0.233279	-0.241594	0.351895	-0.446219
O	-3.592070	0.731816	1.158193	0.056185	-0.000120	-0.031311	-0.004227	0.010913	-0.009415
O	-0.599953	-0.872552	-1.722830	-0.056180	0.212625	0.194063	0.038562	-0.056403	0.070749
C	-1.346250	2.632480	1.467628	0.074043	0.084115	0.004652	0.003681	0.031487	-0.010287
H	-0.498700	3.295480	1.509006	0.004272	-0.017804	-0.009583	0.003215	-0.006019	0.006887
H	-2.192346	2.847933	2.095000	-0.011468	-0.006738	0.002809	-0.011918	0.017374	-0.021850
C	3.802377	0.363460	1.215567	0.088205	0.041504	-0.025510	0.000883	0.006770	0.003656
S	4.582335	1.542342	0.184281	0.133829	-0.089518	0.106996	0.008058	-0.030913	-0.028705
C	3.095674	1.951837	-0.517521	-0.196243	-0.095434	0.094662	0.003008	-0.008915	-0.006303
C	2.052020	1.220865	0.022094	0.148875	0.030071	0.002051	-0.065029	0.336080	0.312275
C	2.468594	0.278635	1.034657	0.014020	0.073712	-0.064311	-0.001981	-0.007948	-0.003078
H	4.404814	-0.208362	1.896057	-0.001876	-0.003765	0.004353	0.000408	-0.002628	-0.003257
H	-0.468767	2.120139	-3.014112	-0.020560	0.004766	-0.024586	-0.003243	-0.001351	-0.004056
H	0.802511	3.102546	-3.729849	-0.012421	-0.002092	-0.022482	-0.011997	-0.002629	-0.009044
C	1.559780	-0.670972	1.744283	0.013699	0.018216	-0.019865	0.001104	0.012028	0.008360
H	1.086731	-1.348202	1.036893	-0.000274	-0.023861	0.003947	-0.003701	0.003889	-0.006998
H	2.111119	-1.263884	2.466497	-0.015886	-0.007308	0.003466	-0.000204	-0.000096	-0.000183
H	0.767368	-0.139187	2.264257	-0.005284	-0.006892	0.024597	0.001733	-0.003180	0.005195
$E(S_0)$		-1164.017188							
$E(S_1)$		-1164.017183							
					CI_{270}				
C	2.660708	2.875264	-1.607496	0.041995	-0.011280	0.018669	-0.003449	0.020267	0.023660
C	1.129404	2.633806	-1.666880	-0.168156	0.057027	-0.023466	-0.056654	0.254043	0.244106
C	0.846638	1.572856	-0.621152	0.096264	-0.066194	-0.087090	0.052757	-0.038803	0.058824
H	2.900500	3.914481	-1.387115	-0.016453	0.009718	-0.014128	0.023571	0.002625	-0.002313
H	3.140201	2.631972	-2.554279	-0.011663	0.007091	-0.023977	-0.023494	-0.005655	-0.002725
H	0.602349	3.530118	-1.335484	0.033021	0.048604	-0.057555	-0.005557	0.045688	-0.040380
C	-0.463952	1.085845	-0.327521	0.226855	-0.228661	-0.296636	-0.043781	0.062356	-0.044466
C	0.610774	2.281184	-3.060682	0.048574	0.040195	0.033609	-0.007269	-0.046288	0.037653
H	1.102457	1.391234	-3.447401	0.006373	-0.007153	-0.001443	0.000763	-0.007048	-0.008503
C	-1.158889	-0.022188	-0.884676	-0.137507	0.199996	0.213539	0.172561	-0.261341	0.325670
C	-2.497822	-0.015217	-0.219432	-0.085990	-0.092157	-0.027909	-0.003204	0.005456	0.001835
O	-2.538095	1.028706	0.645786	0.053793	0.063881	0.023108	0.042447	-0.072985	0.084821
C	-1.329369	1.721270	0.626543	-0.395276	0.226359	0.379087	-0.228405	0.386489	-0.447064
O	-3.406417	-0.767003	-0.369171	0.055416	0.040342	0.003404	-0.001901	0.007926	-0.011131
O	-1.162090	2.682802	1.319725	0.013072	-0.229052	-0.192190	0.031838	-0.069218	0.076261
C	-0.810702	-0.974429	-1.763122	0.095639	-0.011296	-0.056458	-0.008205	0.002233	-0.008847
H	0.164319	-1.000147	-2.219004	-0.002532	0.016420	0.012856	0.001189	-0.002269	0.002265
H	-1.511950	-1.747935	-2.024430	-0.011847	-0.004318	0.005779	-0.008876	0.015061	-0.020891
C	3.792462	0.369351	1.217778	0.093221	0.042228	-0.027361	0.006805	-0.002737	-0.004937
S	4.577629	1.541603	0.180411	0.137264	-0.094459	0.110704	-0.009804	0.028935	0.032321
C	3.092768	1.951401	-0.524886	-0.202166	-0.101868	0.096144	0.001940	0.011368	0.002476
C	2.045370	1.228807	0.019718	0.155153	0.038079	0.005414	0.055596	-0.336643	-0.308810
C	2.456980	0.295285	1.043266	0.013914	0.073678	-0.069531	-0.003428	-0.003154	0.009671
H	4.395186	-0.208952	1.893445	-0.002116	-0.003481	0.005102	-0.000628	0.002530	0.003224
H	-0.458755	2.098188	-3.037211	-0.018824	0.006034	-0.024522	0.001101	0.000838	0.000593
H	0.797574	3.103585	-3.748069	-0.010907	-0.003455	-0.022253	0.011105	-0.000896	0.013780
C	1.550963	-0.651833	1.762187	0.014769	0.018538	-0.021498	0.011796	-0.001784	-0.012175
H	1.066771	-1.320985	1.054262	0.002213	-0.024157	0.007105	-0.001653	-0.005121	-0.000775
H	2.111091	-1.250853	2.472873	-0.016173	-0.005986	0.005105	-0.000224	0.000064	0.000096
H	0.766374	-0.126383	2.300329	-0.007925	-0.004672	0.026391	-0.006940	0.008064	-0.004236
$E(S_0)$		-1164.016796							
$E(S_1)$		-1164.016791							

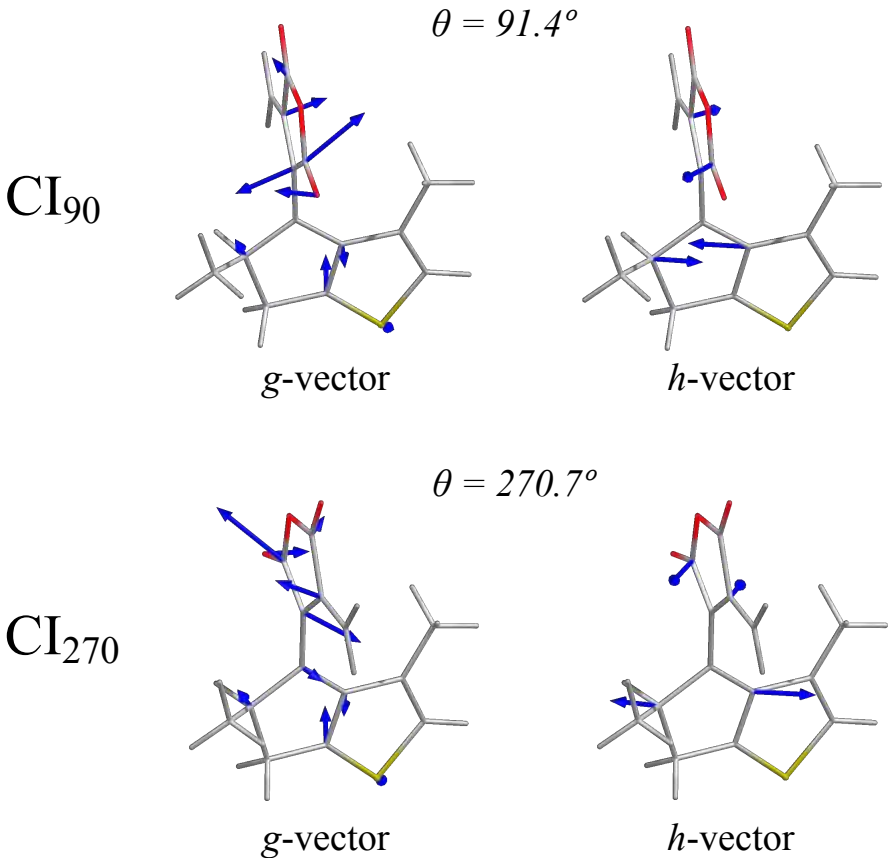

Figure SI-5: Branching plane vectors of the MECI points of DTMF motor. For definition of the central dihedral angle θ, see Scheme 1 of the main text.

7 Total charges of the rotor and the stator blades of DTMF along the S_1 and S_0 MEPs

The total charges on the rotor and the stator blades, see Figure SI-6, were calculated by summing up the Mulliken charges on the respective atoms. The Mulliken charges were calculated from the relaxed SSR density matrices[28] of the S_1 and S_0 states. The relaxed density matrices calculated by the TeraChem® program were saved in the form of the natural orbitals and orbital occupation numbers to an external file in the "molden" format. The SSR natural orbitals were used by the OrbKit suite[54] to obtain the Mulliken charges.

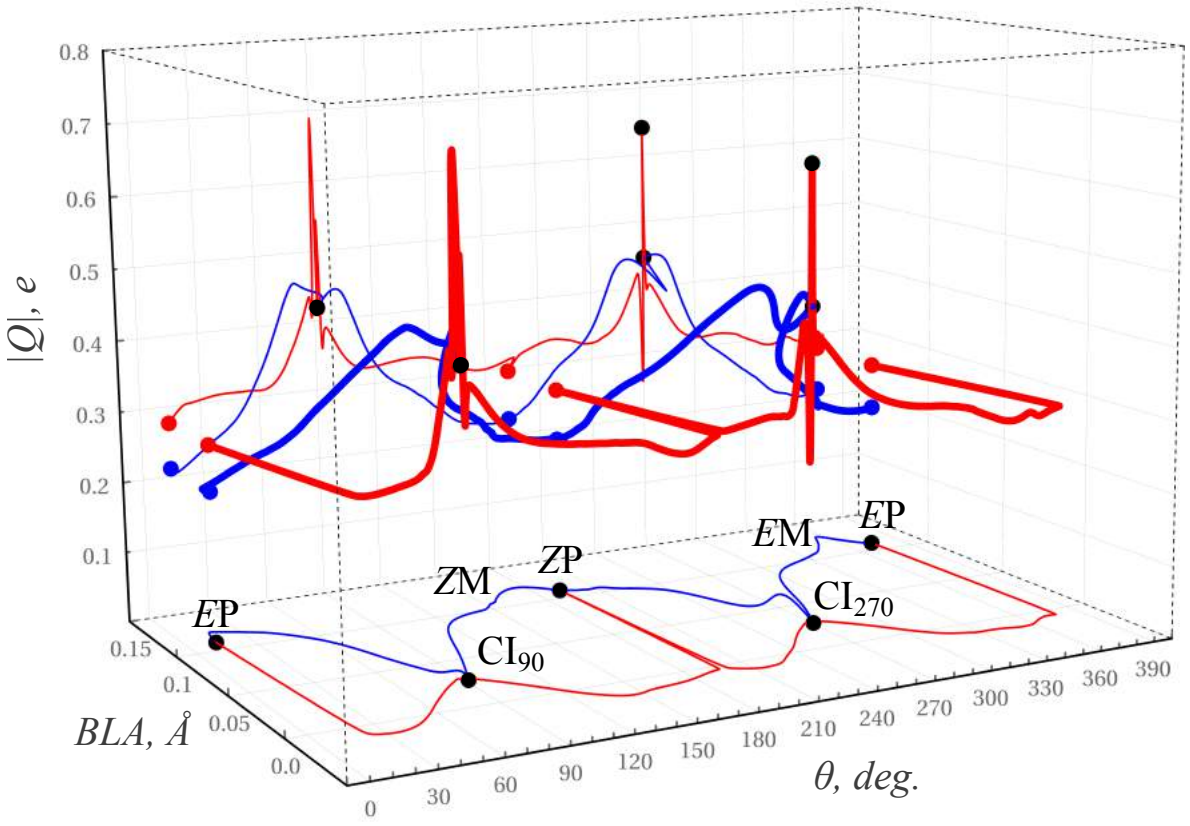

Figure SI-6: Absolute value $|Q|$ of the total charge on the rotor and the stator blades of DTMF along the S_1 (red) and S_0 (blue) MEPS as a function of the central dihedral angle θ (see Scheme 1 for definition) and the BLA distortion.

Near the FC points, the total charge Q indicates that both states, S_1 and S_0, possess covalent character. On the S_0 MEP, the absolute value of the charge Q on the rotor and

the stator steadily increases and near the CIs reaches values of *ca.* 0.45; which indicates heterolytic breaking of the C_4=$C_{3'}$ π-bond. On the S_1 MEP, the charge Q slightly increases as the MEP departs from the FC points (BLA motion) and remains close to ± 0.3; the S_1 state thus retains covalent character. In the proximity of the CIs, the S_1 MEP passes through a narrow region where the S_1 state becomes ionic; $Q \approx \pm 0.5 - 0.6$.

8 Working cycle of the DTMF motor

Using the optimized S_0 minima, the CIs, and the MEPs, the working cycle of the DTMF motor shown in Figure SI-7 is proposed.

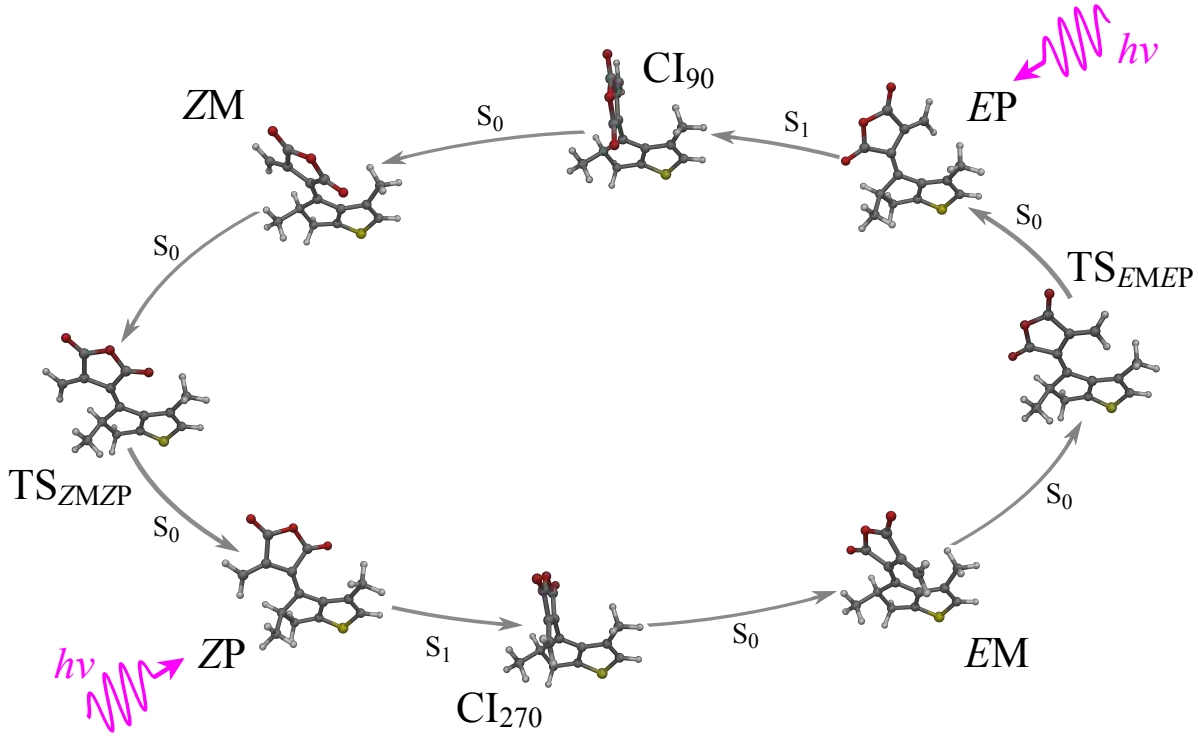

Figure SI-7: Schematic representation of the working cycle of the DTMF motor. The wavy magenta arrows show photoexcitation events.

9 Results of NAMD simulations

Starting from each equilibrium conformation, *E*P and *Z*P, 62 trajectories (31 per each starting point) were prepared by sampling the Wigner function of the respective initial con-

formation. The "*E*P" trajectories were propagated for 384 fs (800 steps) and the "ZP" trajectories for 480 fs (1000 steps). During the propagation all the trajectories underwent transition to the S_0 state.

The products of the photo-reaction were analyzed by visual inspection of the snapshots along the trajectories (taken at each step) and by distribution of the central dihedral angle θ, see Scheme 1 of the main article. The distributions of the central dihedral angle θ at the start and at the end of the *E*P and *Z*P trajectories are shown in Figure SI-8; see also Figure 3 of the main article.

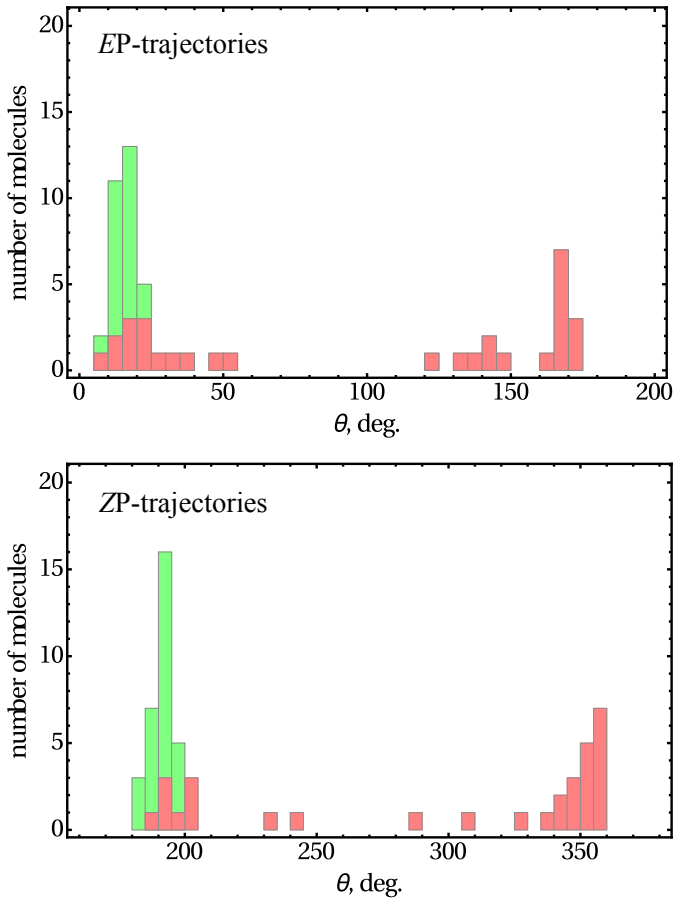

Figure SI-8: Distribution of the central dihedral angle θ at the start of the trajectories (green) and at the end of the trajectories (red). For the values of the dihedral angle θ of the ground state minima and S_1/S_0 CIs, see Figures SI-4 and SI-5, respectively.

At the end of the *E*P trajectories, 14 trajectories fell back to the *E*P conformation and

17 ended up in the ZM conformation; the quantum yield of isomerization is $\phi_{EP\rightarrow ZM}$ = 0.55. Out of the 31 ZP trajectories 10 returned back to the ZP conformation and 21 moved forward to the EM conformation; $\phi_{ZP\rightarrow EM}$ = 0.68.

The distribution of the $S_1 \rightarrow S_0$ hop times for the EP and ZP trajectories is shown in Figure SI-9. The average hop times and the standard deviations, $\langle t \rangle(\sigma_t)$, for the EP and the ZP trajectories are 203(35) fs and 277(53) fs, respectively. The normal distributions with these parameters are shown with blue curves in Figure SI-9.

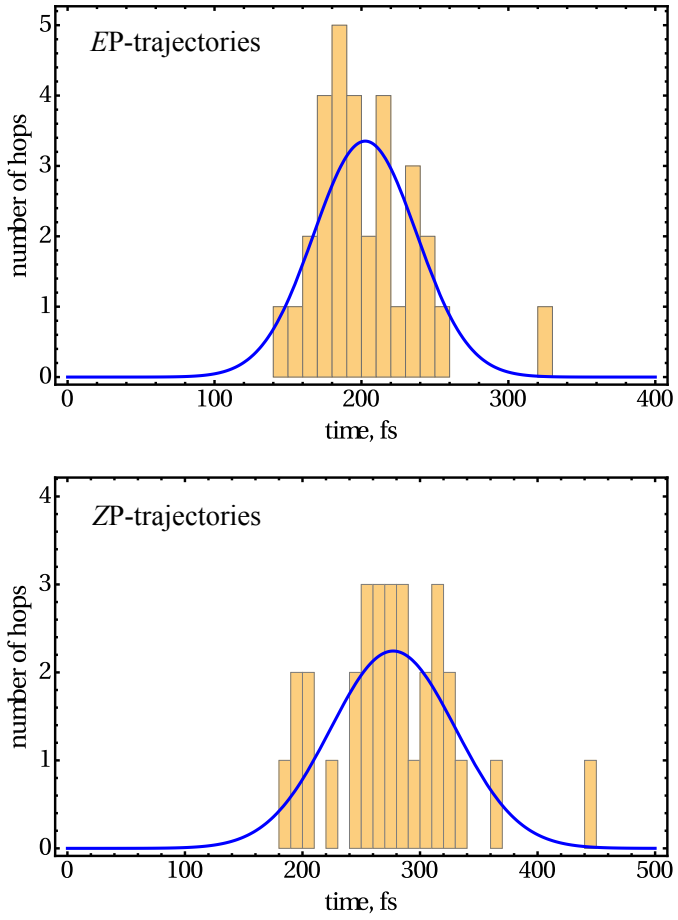

Figure SI-9: Distribution of hop times for the EP (upper panel) and ZP (lower panel) trajectories.

Population of the S_1 state as a function of propagation time was calculated as a fraction of all the trajectories residing in the S_1 state at a given instance t. The S_1 populations for the EP and the ZP trajectories are plotted in Figure SI-10. The populations were fit-

ted by a monoexponential function $f(t) = e^{-\frac{t-t_0}{\tau}}$, where t_0 is the latency time and τ is the exponential decay parameter. Table SI-5 collects the obtained exponential regression parameters as well as the regression coefficients R^2. The monoexponential fits are sufficiently reliable as evidenced by the R^2 values in excess of 0.95. The use of biexponential function for nonlinear regression of the S_1 populations did not lead to any improvement of the monoexponential regression reported in Table SI-5 and Figure SI-10.

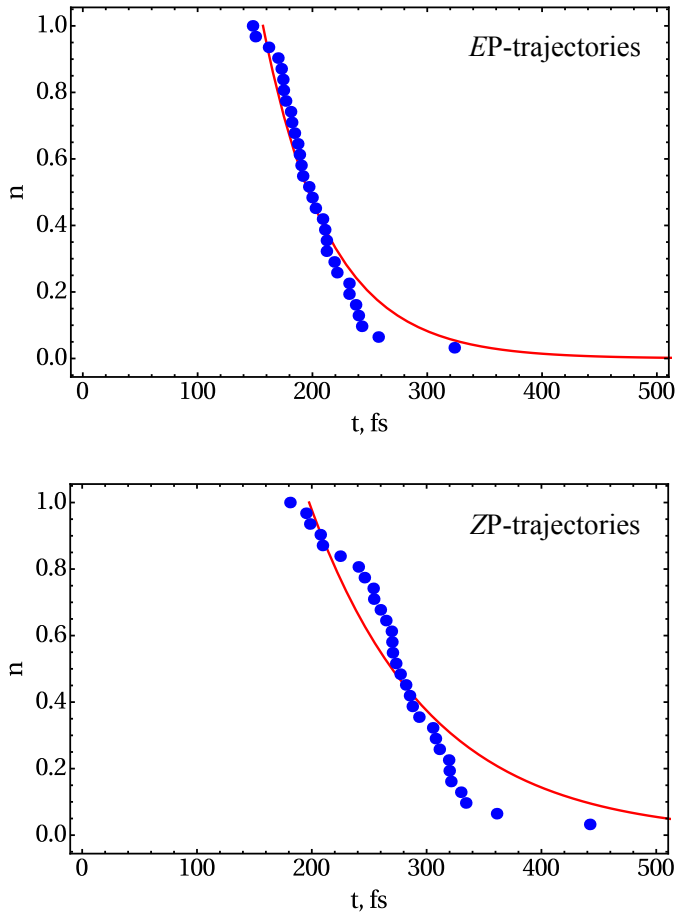

Figure SI-10: Dependence of the S_1 state population n on propagation time for the EP (upper panel) and ZP (lower panel) trajectories. The S_1 populations are shown by blue dots and the exponential fits are shown by the red curves.

Table SI-5: Parameters of the monoexponential fit of the S_1 populations for the *E*P and the *Z*P trajectories. Standard errors of the estimates are given parenthetically. The R^2 parameters of the exponential regression are given in the fourth column.

	t_0, fs	τ, fs	R^2
*E*P trajectories	157(2)	57(4)	0.983
*Z*P trajectories	198(4)	104(8)	0.971

10 Evaluation of the total quantum yield

The full working cycle of the DTMF motor involves two photoisomerizations, both of which have slightly different isomerization quantum yields. Here, we attempt to determine the total quantum yield of the working cycle under a number of simplifying assumptions. First, it is assumed that a quantum is absorbed only when the molecule is in the *E*P or *Z*P conformation. Next, a complete conversion of the M diastereomers to the P form is assumed, *i.e.*, the fraction of the *E*M (or *Z*M) conformation completely converts to *E*P (or *Z*P).

Table SI-6: Fractions of DTMF isomers during full working cycle. The quantum yields of the EP→ZM and ZP→EM photoisomerization reactions are ϕ_1 and ϕ_2, respectively. The fraction of the *E*P isomer is a.

	EP	ZM	ZP	EM
	a	0	$1-a$	0
EP→ZM	$a(1-\phi_1)$	$a\phi_1$	$1-a$	0
ZM→ZP	$a(1-\phi_1)$	0	$1-a+a\phi_1$	0
ZP→EM	$a(1-\phi_1)$	0	$(1-a+a\phi_1)(1-\phi_2)$	$(1-a+a\phi_1)\phi_2$
EM→EP	$a(1-\phi_1)+(1-a+a\phi_1)\phi_2$	0	$(a-a+a\phi_1)(1-\phi_2)$	0

Under these assumptions the fractions of each isomer of DTMF at each step (stroke) of the working cycle are collected in Table SI-6. The quantum yields of the EP→ZM and ZP→EM photoisomerization reactions are denoted as ϕ_1 and ϕ_2 and the fractions of the *E*P and *Z*P isomers are a and $1-a$, respectively. We are interested how large a fraction of the *E*P conformation carries out full revolution at the end of the working cycle. From the assumption of 100% efficiency of the thermal step and from the fraction of the *E*M isomer at the end of the second photostep it follows that the $(1-a+a\phi_1)\phi_2$ fraction of *E*P conformer performs the full revolution (fifth column in the fourth row in Table SI-6). The equilibrium fraction of the *E*P conformation can be found by equating the initial fraction a of *E*P with its fraction at the end of the cycle, *i.e.*, the last row of the second column in Table SI-6, $a = a(1-\phi_1)+(1-a+a\phi_1)\phi_2$. This yields $a = \frac{\phi_2}{\phi_1+\phi_2-\phi_1\phi_2}$. Substituting this

value to $(1 - a + a\phi_1)\phi_2$ yields

$$\Phi = \frac{1}{2}\frac{\phi_1\phi_2}{\phi_1 + \phi_2 - \phi_1\phi_2}\,, \tag{SI-11}$$

where the $1/2$ prefactor follows from the fact that two quanta were absorbed per revolution. The theoretical upper limit of Φ is 0.5, *i.e.*, one revolution per two quanta; it can be achieved only if $\phi_1 = \phi_2 = 1$. For the DTMF motor with $\phi_1 = 0.55$ and $\phi_2 = 0.68$, the total quantum yield $\Phi = 0.22$. For a motor with quantum efficiency of both photoisomerization steps not exceeding 0.3, the total quantum yield is below 0.09.

11 Multimedia files

The following multimedia files are available:

1) Cartoon (dtmf-mep-cycle.gif) showing animated geometric transformations occurring along the working cycle of the DTMF motor (highlighted in Figure 2 of the main article), see also Figure SI-7 of the Supporting Information.

2) Animation (dtmf-ep-frwd.gif) of the forward propagating trajectories (EP $\rightarrow$ ZM) starting in the EP conformation.

3) Animation (dtmf-ep-back.gif) of the backward propagating trajectories (EP $\rightarrow$ EP) starting in the EP conformation.

4) Animation (dtmf-zp-frwd.gif) of the forward propagating trajectories (ZP $\rightarrow$ EM) starting in the ZP conformation.

5) Animation (dtmf-zp-back.gif) of the backward propagating trajectories (ZP $\rightarrow$ ZP) starting in the ZP conformation.

References

(1) Ewen, J. A.; Elder, M. J.; Jones, R. L. Patent No.: US 6,635,779 Date of Patent: Oct. 21, 2003.

(2) Pinna, G.; Curzu, M. M.; Dore, A.; Lazzari, P.; Ruiu, S.; Pau, A.; Murineddu, G.; Pinna, G. A. Tricyclic pyrazoles part 7. Discovery of potent and selective dihydrothienocyclopentapyrazole derived CB2 ligands. *Eur. J. Med. Chem.* **2014**, *85*, 747–757.

(3) Sun, Z.; Hosmane, R. S.; Tadros, M. Fulgides and photochromism. Synthesis of (E)- and (Z)-5-dicyanomethylene-4-dicyclopropylmethylene-3-[1-(2,5-dimethyl-3-furyl)ethylidene] tetrahydrofuran-2-one. *Tetrahedron Lett.* **1995**, *36*, 3453 – 3456.

(4) Ryabov, A. N.; Gribkov, D. V.; Izmer, V. V.; Voskoboynikov, A. Z. Zirconium Complexes with Cyclopentadienyl Ligands Involving Fused a Thiophene Fragment. *Organometallics* **2002**, *21*, 2842–2855.

(5) Fernández Landaluce, T.; London, G.; Pollard, M. M.; Rudolf, P.; Feringa, B. L. Rotary Molecular Motors: A Large Increase in Speed through a Small Change in Design. *J. Org. Chem.* **2010**, *75*, 5323–5325.

(6) Strübe, F.; Siewertsen, R.; Sönnichsen, F. D.; Renth, F.; Temps, F.; Mattay, J. Photochromism of Rotation-Hindered Furylfulgides Influenced by Steric Modifications. *Eur. J. Org. Chem. 2011*, 1947–1955.

(7) Zmeeva, S. Y.; Rybalkin, V. P.; Popova, L. L.; Tkachev, V. V.; Revinskii, Y. V.; Tikhomirova, K. S.; Starikov, A. G.; Dubonosov, A. D.; Bren, V. A.; Aldoshin, S. M. et al. Photochromism of novel [1]benzothien-2-yl fulgides. *Tetrahedron* **2016**, *72*, 5776 – 5782.

(8) Weerasekara, R. K.; Uekusa, H.; Hettiarachchi, C. V. Multicolor Photochromism of Fulgide Mixed Crystals with Enhanced Fatigue Resistance. *Cryst. Growth Des.* **2017**, *17*, 3040–3047.

(9) Filatov, M.; Olivucci, M. Designing conical intersections for light-driven single molecule rotary motors: From precessional to axial motion. *J. Org. Chem.* **2014**, *79*, 3587–3600.

(10) Kaftory, M. Photochromic and thermochromic compounds. I. Structures of (E) and (Z) isomers of 2-isopropylidene-3-[1-(2-methyl-5-phenyl-3-thienyl)ethylidene]succinic anhydride, C20H18O3S, and the photoproduct 7,7a-dihydro-4,7,7,7a-tetramethyl-2-phenylbenzo[b]thiophene-5,6-dicarboxylic anhydride (P), C20H18O3S. *Acta Crystallogr. Sec. C* **1984**, *40*, 1015–1019.

(11) Yokoyama, Y. Fulgides for Memories and Switches. *Chem. Rev.* **2000**, *100*, 1717–1740.

(12) Filatov, M.; Shaik, S. A spin-restricted ensemble-referenced Kohn-Sham method and its application to diradicaloid situations. *Chem. Phys. Lett.* **1999**, *304*, 429–437.

(13) Moreira, I. d. P. R.; Costa, R.; Filatov, M.; Illas, F. Restricted ensemble-referenced Kohn-Sham versus broken symmetry approaches in density functional theory: Magnetic coupling in Cu binuclear complexes. *J. Chem. Theory Comput.* **2007**, *3*, 764–774.

(14) Kazaryan, A.; Heuver, J.; Filatov, M. Excitation Energies from Spin-Restricted Ensemble-Referenced Kohn-Sham Method: A State-Average Approach. *J. Phys. Chem. A* **2008**, *112*, 12980–12988.

(15) Filatov, M. Assessment of density functional methods for obtaining geometries at conical intersections in organic molecules. *J. Chem. Theory Comput.* **2013**, *9*, 4526–4541.

(16) Filatov, M. Spin-restricted ensemble-referenced Kohn-Sham method: basic principles and application to strongly correlated ground and excited states of molecules. *WIREs Comput. Mol. Sci.* **2015**, *5*, 146–167.

(17) Filatov, M. In *Density-functional methods for excited states*; Ferré, N., Filatov, M., Huix-Rotllant, M., Eds.; Top. Curr. Chem.; Springer: Heidelberg, 2016; Vol. 368; pp 97–124.

(18) Valone, S. M. A one-to-one mapping between one-particle densities and some n-particle ensembles. *J. Chem. Phys.* **1980**, *73*, 4653–4655.

(19) Lieb, E. H. Density functionals for Coulomb systems. *Int. J. Quantum Chem.* **1983**, *24*, 243–277.

(20) Perdew, J. P.; Parr, R. G.; Levy, M.; Balduz Jr., J. L. Density-Functional Theory for Fractional Particle Number: Derivative Discontinuities of the Energy. *Phys. Rev. Lett.* **1982**, *49*, 1691–1694.

(21) Englisch, H.; Englisch, R. Hohenberg-Kohn Theorem and Non-V-Representable Densities. *Physica* **1983**, *A121*, 253–268.

(22) Englisch, H.; Englisch, R. Exact Density Functionals for Ground-State Energies. I. General Results. *Phys. Stat. Sol. (b)* **1984**, *123*, 711–721.

(23) Englisch, H.; Englisch, R. Exact Density Functionals for Ground-State Energies II. Details and Remarks. *Phys. Stat. Sol. (b)* **1984**, *124*, 373–379.

(24) Gross, E. K. U.; Oliveira, L. N.; Kohn, W. Rayleigh-Ritz variational principle for ensembles of fractionally occupied states. *Phys. Rev. A* **1988**, *37*, 2805–2808.

(25) Gross, E. K. U.; Oliveira, L. N.; Kohn, W. Density-functional theory for ensembles of fractionally occupied states. I. Basic formalism. *Phys. Rev. A* **1988**, *37*, 2809–2820.

(26) Oliveira, L. N.; Gross, E. K. U.; Kohn, W. Density-functional theory for ensembles of fractionally occupied states. II. Application to the He atom. *Phys. Rev. A* **1988**, *37*, 2821–2833.

(27) Oliveira, L. N.; Gross, E. K. U.; Kohn, W. Ensemble-Density Functional Theory. *Int. J. Quantum Chem.: Quantum Chem. Symp.* **1990**, *24*, 707–716.

(28) Filatov, M.; Liu, F.; Martínez, T. J. Analytical derivatives of the individual state energies in ensemble density functional theory method. I. General formalism. *J. Chem. Phys.* **2017**, *147*, 034113.

(29) Ha, J.-K.; Lee, I. S.; Min, S. K. Surface Hopping Dynamics beyond Nonadiabatic Couplings for Quantum Coherence. *J. Phys. Chem. Lett.* **2018**, *9*, 1097–1104.

(30) Hunter, G. Conditional probability amplitudes in wave mechanics. *Int. J. Quantum Chem.* **1975**, *9*, 237–242.

(31) Abedi, A.; Maitra, N. T.; Gross, E. K. U. Exact factorization of the time-dependent electron-nuclear wave function. *Phys. Rev. Lett.* **2010**, *105*, 123002.

(32) Abedi, A.; Maitra, N. T.; Gross, E. K. U. Correlated electron-nuclear dynamics: Exact factorization of the molecular wave-function. *J. Chem. Phys.* **2012**, *137*, 22A530.

(33) Abedi, A.; Agostini, F.; Suzuki, Y.; Gross, E. K. U. Dynamical steps that bridge piecewise adiabatic shapes in the exact time-dependent potential energy surface. *Phys. Rev. Lett.* **2013**, *110*, 263001.

(34) Agostini, F.; Abedi, A.; Suzuki, Y.; Min, S. K.; Maitra, N. T.; Gross, E. K. U. The exact electronic back-reaction on classical nuclei in non-adiabatic charge transfer. *J. Chem. Phys.* **2015**, *142*, 084303.

(35) Tully, J. C. Molecular dynamics with electronic transitions. *J. Chem. Phys.* **1990**, *93*, 1061.

(36) Granucci, G.; Persico, M.; Zoccante, A. Including quantum decoherence in surface hopping. *J. Chem. Phys.* **2010**, *133*, 134111.

(37) Hammes-Schiffer, S.; Tully, J. C. Proton transfer in solution: Molecular dynamics with quantum transitions. *J. Chem. Phys.* **1994**, *101*, 4657–4667.

(38) Ufimtsev, I. S.; Martínez, T. J. Quantum Chemistry on Graphical Processing Units. 1. Strategies for two-electron integral evaluation. *J. Chem. Theory Comput.* **2008**, *4*, 222–231.

(39) Ufimtsev, I. S.; Martínez, T. J. Quantum Chemistry on Graphical Processing Units. 2. Direct Self-Consistent-Field (SCF) Implementation. *J. Chem. Theory Comput.* **2009**, *5*, 1004–1015.

(40) Ufimtsev, I. S.; Martínez, T. J. Quantum Chemistry on Graphical Processing Units. 3. Analytical Energy Gradients and First Principles Molecular Dynamics. *J. Chem. Theory Comput.* **2009**, *5*, 2619–2628.

(41) Ufimtsev, I. S.; Martínez, T. J. Graphical Processing Units for Quantum Chemistry. *Comput. Sci. Eng.* **2008**, *10*, 26–34.

(42) Titov, A. V.; Ufimtsev, I. S.; Luehr, N.; Martínez, T. J. Generating Efficient Quantum Chemistry Codes for Novel Architectures. *J. Chem. Theory Comput.* **2013**, *9*, 213–221.

(43) Song, C.; Wang, L.-P.; Martínez, T. J. Automated Code Engine for Graphical Processing Units: Application to the Effective Core Potential Integrals and Gradients. *J. Chem. Theory Comput.* **2016**, *12*, 92–106.

(44) Krishnan, R.; Binkley, J. S.; Seeger, R.; Pople, J. A. Self-consistent molecular orbital methods. XX. A basis set for correlated wave functions. *J. Chem. Phys.* **1980**, *72*, 650–654.

(45) Becke, A. D. Density-Functional Exchange-Energy Approximation with Correct Asymptotic Behavior. *Phys. Rev. A* **1988**, *38*, 3098–3100.

(46) Lee, C.; Yang, W.; Parr, R. G. Development of the Colle-Salvetti Correlation-Energy Formula into a Functional of the Electron Density. *Phys. Rev. B* **1988**, *37*, 785–789.

(47) Becke, A. D. A New Mixing of Hartree-Fock and Local Density-Functional Theories. *J. Chem. Phys.* **1993**, *98*, 1372–1377.

(48) Kästner, J.; Carr, J. M.; Keal, T. W.; Thiel, W.; Wander, A.; Sherwood, P. DL-FIND: An Open-Source Geometry Optimizer for Atomistic Simulations. *J. Phys. Chem. A* **2009**, *113*, 11856–11865.

(49) Levine, B.; Coe, J. D.; Martínez, T. J. Optimizing conical intersections without derivative coupling vectors: application to multistate multireference second-order perturbation theory (MS-CASPT2). *J. Phys. Chem. B* **2008**, *112*, 405–413.

(50) Jónsson, H.; Mills, G.; Jacobsen, K. W. In *Classical and Quantum Dynamics in Condensed Phase Simulations*; Berne, B. J., Ciccotti, G., Coker, D. F., Eds.; World Scientific: Singapore, 1998; Chapter 16, pp 385–404.

(51) Oppenheim, I.; Ross, J. Temperature Dependence of Distribution Functions in Quantum Statistical Mechanics. *Phys. Rev.* **1957**, *107*, 28–32.

(52) Davies, R. W.; Davies, K. T. R. On the Wigner Distribution Function for an Oscillator. *Ann. Phys.* **1975**, *89*, 261–273.

(53) Lan, Z.; Lu, Y.; Weingart, O.; Thiel, W. Nonadiabatic Decay Dynamics of a Benzylidene Malononitrile. *J. Phys. Chem. A* **2012**, *116*, 1510–1518.

(54) Hermann, G.; Pohl, V.; Tremblay, J. C.; Paulus, B.; Hege, H.-C.; Schild, A. ORBKIT: A Modular Python Toolbox for Cross-Platform Postprocessing of Quantum Chemical Wavefunction Data. *J. Comput. Chem.* **2016**, *37*, 1511–1520.